

# The Weak Shock in the Core of the Perseus Cluster

J. Graham<sup>1</sup>\*, A.C. Fabian<sup>1</sup> and J.S. Sanders<sup>1</sup>

<sup>1</sup> Institute of Astronomy, Madingley Road, Cambridge

3 June 2018

## ABSTRACT

The dissipation of energy from sound waves and weak shocks is one of the most promising mechanisms for coupling AGN activity to the surrounding intracluster medium (ICM), and so offsetting cooling in cluster cores. We present a detailed analysis of the weak shock found in deep *Chandra* observations of the Perseus cluster core. A comparison of the spectra either side of the shock front shows that they are very similar. By performing a deprojection analysis of a sector containing the shock, we produce temperature and density profiles across the shock front. These show no evidence for a temperature jump coincident with the density jump. To understand this result, we model the shock formation using 1D hydrodynamic simulations including models with thermal conduction and  $\gamma < 5/3$  gas. These models do not agree well with the data, suggesting that further physics is needed to explain the shock structure. We suggest that an interaction between the shock and the H $\alpha$  filaments could have a significant effect on cooling the post-shock gas.

We also calculate the thermal energy liberated by the weak shock. The total energy in the shocked region is about 3.5 times the work needed to inflate the bubbles adiabatically, and the power of the shock is around  $6 \times 10^{44}$  erg s $^{-1}$  per bubble, just over  $10^{45}$  erg s $^{-1}$  in total.

**Key words:** X-rays: galaxies — galaxies: clusters: individual: Perseus — intergalactic medium — cooling flows

## 1 INTRODUCTION

The baryonic content of galaxy clusters is dominated by a hot  $10^7 - 10^8$  K plasma—the IntraCluster Medium (ICM)—which radiates via bremsstrahlung and line emission processes, making clusters luminous X-ray sources. Observationally the population of clusters can naturally be divided into two classes; *cool-core* clusters which show a bright central peak in their surface brightness and *non-cool-core* clusters which do not show sharply peaked emission. It is believed that the different structure of the two classes is a result of different merger histories, with cool-core clusters being more relaxed structures which have developed their dense cores without significant disruption.

Measurements of the central luminosities of cool-core clusters show that they have cooling times much shorter than the age of the universe. This led to the development of the cooling flow model (see Fabian 1994 for a review) in which the cooling of gas in central regions causes it to lose pressure support creating an inflow of gas toward the centre. The cooled gas was expected to be observed both as low temperature X-ray emitting gas and as cold gas in the nucleus of the cluster. However it has long been known that the star formation rates in central cluster galaxies are below the rate expected in the cooling flow picture and, with the launch of the latest generation of X-ray satellites, it has been confirmed that observed rates of mass deposition from the hot phase are much

smaller than the expected for a cooling flow (Peterson et al. 2001, 2003), with the core temperature typically falling to about a third of the virial temperature. Instead, it is generally accepted that there is some heat source counteracting the cooling of the X-ray gas. The nature of this heat source is still an open question but the Active Galactic Nucleus (AGN) in the cluster centre has emerged as the leading contender.

Observationally, the centres of cool-core clusters often show highly disrupted morphologies, in contrast to their overall smooth profile. Many cool-core clusters show “bubbles”—regions with depressed X-ray surface brightness profiles indicating that they are cavities in the ICM. These cavities are filled with relativistic plasma and are evacuated by relativistic jets produced by accretion onto the central AGN, thereby coupling the gravitational energy released within a few Schwarzschild radii of the central black hole with the cool-core region which has a typical diameter of  $\sim 100$  kpc. Since the rate of AGN accretion is presumably related to the mass drop out rate from the ICM, AGN heating has the potential to be self-regulating, thus explaining the ubiquity of cool-core clusters.

Recent studies of the volumes of observed cavities have found that the  $p\delta V$  work done in inflating the cavities is, in most cases, sufficient to offset the X-ray cooling of the cluster gas (Birzan et al. 2004, 2006; Dunn & Fabian 2006; Rafferty et al. 2006). A natural consequence of the expansion of these bubbles is the formation of a shock wave which carries the work done in expanding the bubbles away from the cluster core. Weak shocks have been observed in

\* E-mail:j.graham@ast.cam.ac.uk

several nearby clusters, including Perseus (Fabian et al. 2006) and Virgo (Forman et al. 2007).

Further evidence of weak shocks is seen in the Perseus cluster as ripples in the surface brightness (Fabian et al. 2003a, 2006). These are interpreted to be low-amplitude sound waves propagating through the cluster. That there are more ripples observed than bubbles may be an indication that the expansion of the bubble is not uniform.

The dissipation of weak shock waves at the cluster centre has been investigated by Mathews et al. (2006) and Fujita & Suzuki (2006). These authors both use one-dimensional ideal gas models to conclude that weak shocks dissipate over a small region compared to the cooling radius of the cluster and find temperature profiles that are centrally peaked, not centrally decreasing as observed in real clusters. Nevertheless, the fact that weak shocks and ripples are indeed observed implies that the physics of real cluster cores must be more complex than is assumed in these models.

One of the most surprising conclusions in the deep study of the Perseus Cluster (Fabian et al. 2006) was that the weak shock in Perseus is isothermal; they found no evidence for the  $\sim 25$  percent jump in temperature across the shock expected from the observed density jump. Moreover, multi-temperature fits showed proportionally more cool (2 keV) gas inside the shock than outside, strongly suggesting that physics beyond that of a simple ideal gas is needed to understand the structure of the shock and hence energy dissipation in cluster cores. Here we present a more detailed study of the data first presented in Fabian et al. (2006), concentrating on the region around the inner bubbles in Perseus, including modelling of the shock wave evolution. We adopt the same cosmological parameters as in that paper; in particular we assume  $H_0 = 71 \text{ km s}^{-1} \text{ Mpc}^{-1}$ .

## 2 STRUCTURE OF THE SHOCK

The analysis of the shock front in Fabian et al. (2006) was based on a projected view of the regions inside and outside of the shock. Whilst this analysis has the significant advantage that it does not require any assumptions about the (unknown) geometry of the cluster, the projected gas can have a significant influence on the results and, in particular, makes comparison with simulation difficult. To get around this, we have reanalysed the dataset of Fabian et al. (2006) in the sector shown in Fig. 1 performing a deprojection analysis.

### 2.1 Surface Brightness Profile

Fig. 2 shows the projected and deprojected surface brightness profile in the sector. The sector used to generate the profile here was quite wide ( $80^\circ$ ). In some places the edge of the shock appears to be better defined. We examined several sectors ranging down to  $8.9^\circ$ , carefully making sure the sector was aligned along the edge of the shock, but the width of the shock appeared to remain consistent.

### 2.2 Temperature Profile

Fig. 3 shows the temperature and density profiles deprojected in 0.1 arcmin (2.2 kpc) annuli, using the spectral deprojection method of Sanders & Fabian (2007). This is a simple method to calculate deprojected count spectra from observed spectra. Working from the outside of the cluster, deprojected count spectra are calculated by subtracting from the observed projected spectrum the

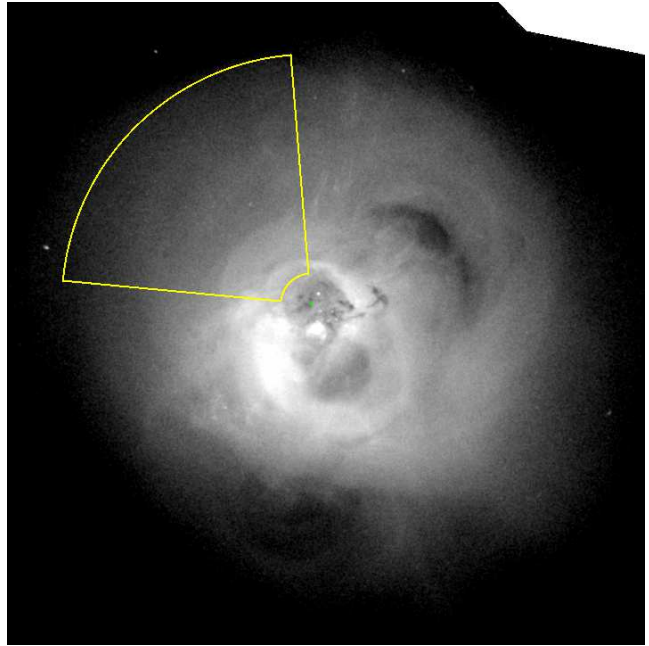


**Figure 1.** The sector of the Perseus cluster used in the deprojection analysis shown on the *Chandra* surface brightness image of the cluster core. The sector is chosen to exclude the regions affected by cooler projected emission. The centre of the sector is positioned so that the shock front is at constant radius, placing the centre of the sector at the centre of the bubble.

contribution from those shells which lie between the emitting region and the observer. Further details of the deprojection method, including a comparison with other deprojection codes such as PROJECT will be provided in a future paper (Sanders, et al., in prep.). For our analysis the spectra have been grouped to a minimum of 100 counts per spectral bin in the outside annulus, with the others having the same binning. Spectral fits are performed by minimising the  $\chi^2$  statistic, with the temperature, column density, abundance and normalisation held free, and the redshift frozen at 0.0183.

At the shock front, the density jumps by a factor  $1.31 \pm 0.04$ . The Mach number and expected temperature jump can then be derived from the Rankine-Hugoniot relations, assuming the curvature of the shock front has a negligible effect. With  $\gamma = 5/3$ , appropriate if the ICM is gas (as opposed to cosmic ray) dominated, the Mach number of the shock is  $1.21 \pm 0.03$  and the expected temperature jump a factor  $1.27 \pm 0.03$ .

In the deprojected temperature profile, it is apparent that there is no significant temperature jump between the first preshock annulus and the first postshock annulus. The temperature ratio is  $1.03 \pm 0.06$ . This is clearly inconsistent with the prediction of a purely hydrodynamic model.

Although there is no temperature jump at the shock, there is some evidence for a temperature peak  $\sim 3$  kpc behind the shock front. The ratio of this maximum in the postshock temperature and the minimum of the preshock temperature is  $1.14 \pm 0.07$ , which is marginally consistent with either a flat profile or a standard shock jump. However, interpreting this feature as a standard shock requires some process beyond simple hydrodynamics to explain the offset between the shock face and the temperature jump.

The annulus centred around 11.8 kpc, shows a drop in both the temperature and the density, corresponding to a drop in the gas pressure. The origin of such a drop is not well understood; it suggests an additional non-thermal contribution to the pressure

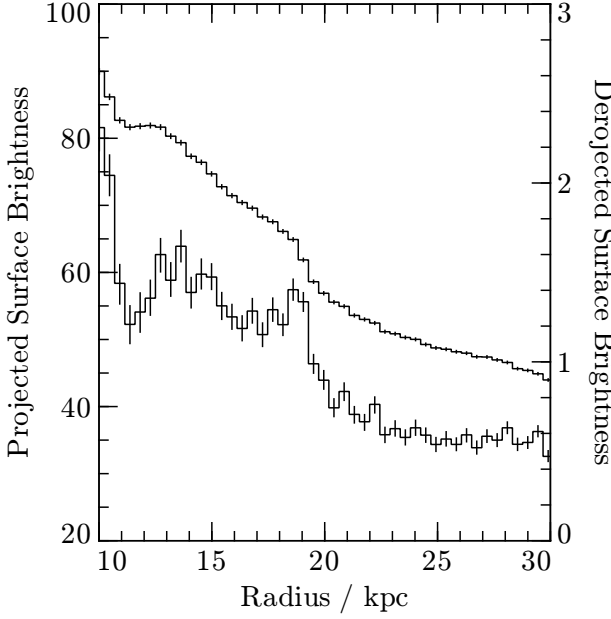


**Figure 2.** Projected (upper curve) and deprojected (lower curve) surface brightness profile in the sector of the Perseus cluster in Fig. 1. The units are arbitrary.

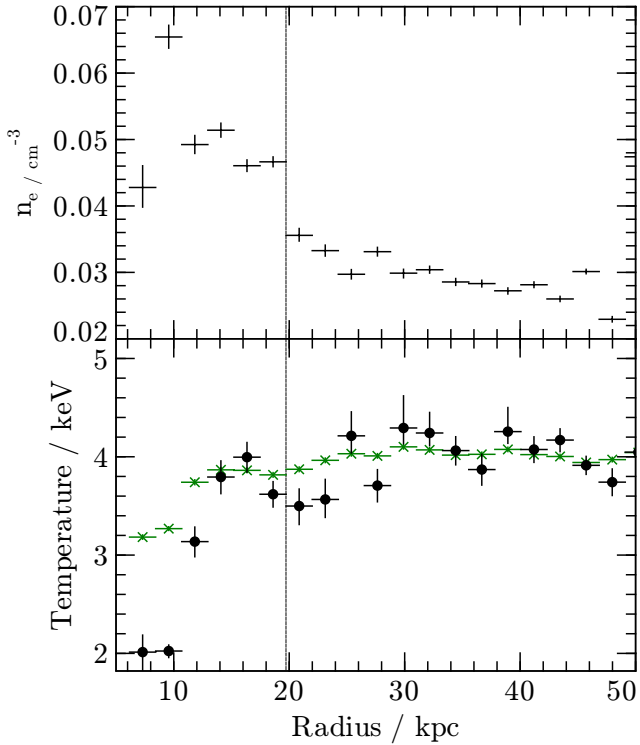


**Figure 3.** Electron density (top) and projected and deprojected (circles) temperature profiles (bottom) in the NE sector of Perseus. Radii are measured relative to the centre of the sector. The dotted line shows the position of the shock.

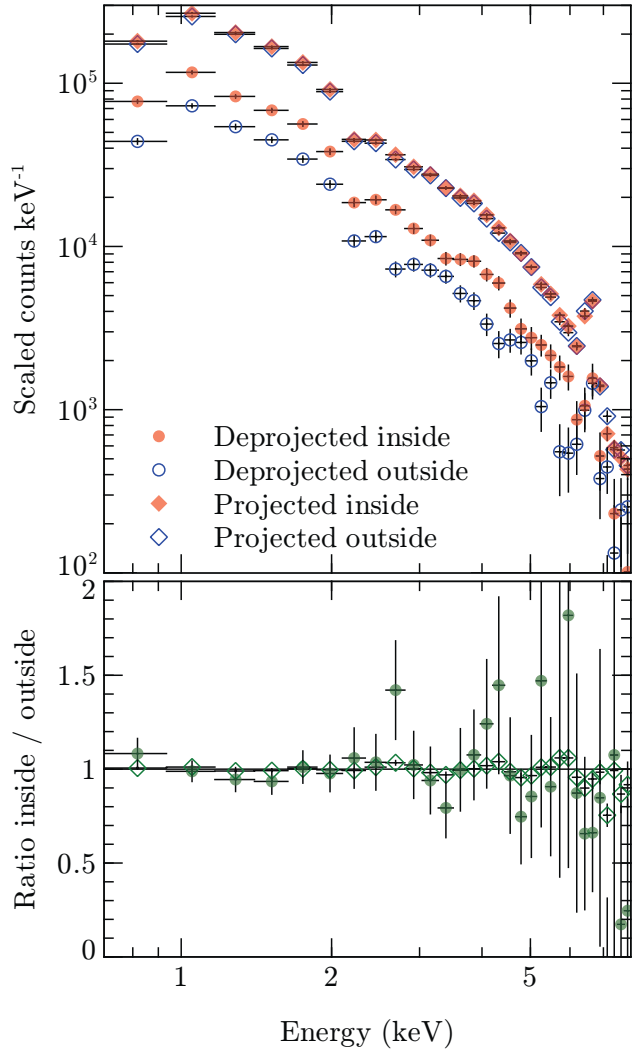


**Figure 4.** Comparison of the projected (diamonds) and deprojected (circles) spectra in the immediately inside (filled red points) and immediately outside the shock (unfilled blue points). The projected spectra are presented without any scaling, whilst the deprojected counts (circles) are scaled to units of  $10^{-5}$  counts  $s^{-1} \text{arcmin}^{-2} \text{keV}$ , to take into account the area of the sector. The ratio plot (bottom) gives the ratio of the counts per unit energy inside the shock to those outside, scaled to have the same overall normalisation. The projected spectra inside and outside the shock show remarkable consistency.

from e.g. magnetic fields, cosmic rays, or ram pressure in this region. Taking only points outside this, the overall temperature profile shows evidence for some structure with a constant model providing a poor fit (reduced  $\chi^2 = 2.7$ ).

Accounting for the need to fit both the actual structure of the shock front, and the fact that the temperature profile far in front and behind the shock is not well modelled, we choose to proceed by comparing models profiles to the temperature points in the region, 16 – 25 kpc. This encompasses two annuli inside and three annuli outside the shock.

### 2.2.1 Checks on the Deprojection Analysis

In order to check that the low apparent temperature jump behind the shock is not an artifact of the deprojection procedure, we have

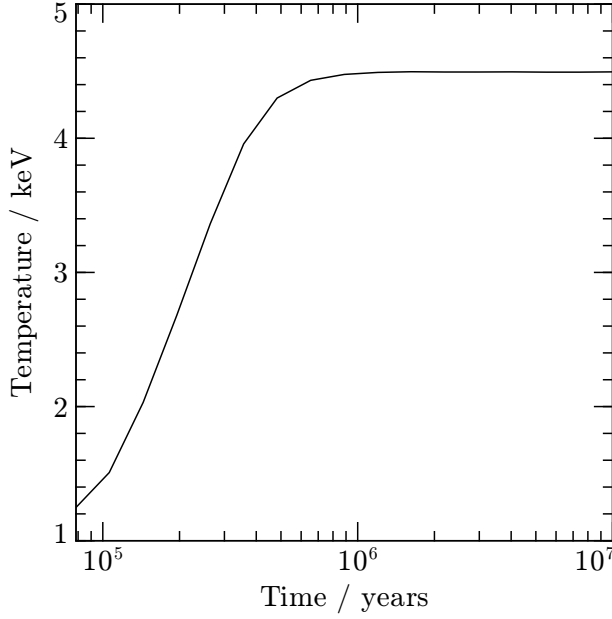


**Figure 5.** Fitted temperature for NEI models with  $n_e = 0.03$  and  $T = 4.5$  keV at various times after the shock has passed.

compared the spectra from the annuli either side of the shock front. Fig. 4 shows the projected and deprojected spectra from regions immediately inside and outside the shock front. The spectra on each side of the shock are remarkably similar, both in projection and in deprojection, consistent with the small temperature jump found from the full deprojection analysis.

An additional test we made was to use the spectrum from outside the shock as a background for the shocked region. This is almost certainly an overestimate for the amount of emission projected onto the shocked region. Using this background, the measured temperature was still compatible with our deprojected results. It appears not to matter how much projected emission is subtracted from the shocked region as the spectra are almost identical.

### 2.2.2 Non-Equilibrium Ionisation

The models fitted above assume that the ions in each zone are in their equilibrium ionisation state. Following the rapid temperature change induced by the passage of a shock, there is a finite time before ionisation equilibrium is re-established. During this time, the temperature inferred from X-ray spectral fitting will be lower than the actual gas temperature, suggesting a possible explanation for the offset of the temperature jump at the shock front. This was tested using the XSPEC NEI model (Hamilton et al. 1983; Borkowski et al. 1994; Liedahl et al. 1995; Borkowski et al. 2001) with a PHABS absorbed component to simulate *Chandra* observations at various times after the shock passage and fitting the simulated data with the EQUIL model. The temperature fitted to these models is shown in Fig. 5; clearly at  $t = 10^6$  yr the fitted temperature is equal to the input temperature. Since the shock velocity is approximately  $1 \text{ kpc}/10^6 \text{ yr}$  non-equilibrium ionisation effects can account for an offset of no-more than 1 kpc, indicating that non-ionisation equilibrium alone is not enough to explain the apparent density/temperature offset at the shock front.

## 3 MODELLING AGN-INDUCED WEAK SHOCKS

### 3.1 Equations of fluid dynamics

For the purposes of our model, we assumed the dynamics of the ICM are those of a single phase, inviscid fluid in which magnetic fields are too weak to be dynamically important and where the electron-ion coupling time is much shorter than any timescale of interest. In this case the equations describing the evolution of the ICM are those of ideal hydrodynamics (e.g. Landau & Lifshitz 1959):

$$\frac{D\rho}{Dt} + \rho \nabla \cdot u = 0 \quad (1)$$

$$\rho \frac{Du}{Dt} = -\nabla p - \rho g \quad (2)$$

$$\frac{D\epsilon}{Dt} + p \frac{D\left(\frac{1}{\rho}\right)}{Dt} = -\frac{1}{\rho} \nabla \cdot (\kappa \nabla T) \quad (3)$$

where  $D \equiv \frac{\partial}{\partial t} + u \cdot \nabla$  is the total (Lagrangian) derivative,  $u$  is the fluid velocity,  $p$  the pressure,  $\rho$  the density,  $\epsilon$  the specific internal energy,  $T$  the temperature, and  $\kappa$  the conductivity. For a fully ionised hydrogen plasma, the conductivity  $\kappa$  is given by (Spitzer 1956):

$$\kappa = 640\epsilon\delta_T \left(\frac{2\pi}{m_e}\right)^{1/2} \frac{k_B\epsilon_0^2}{e^4} \frac{(k_B T)^{5/2}}{Z \ln \Lambda} \quad (4)$$

where  $Z$  is the charge of the ion,  $\Lambda$  is the Coulomb logarithm with  $\ln \Lambda \approx 37$  in the conditions of interest,  $\epsilon \approx 0.4$  accounts for the reduction of conductivity in a plasma due to the electric field and  $\delta_T \approx 0.225$  accounts for the finite proton mass. The remaining symbols have their usual physical meanings.

In the case of a steep temperature gradient and strong conductivity, the rate of heat flow predicted from the bulk description above can exceed the maximum rate at which the electrons are able to transport energy. In this case it is appropriate to replace the conduction term in the energy equation (3) by one appropriate for saturated conductivity (Cowie & McKee 1977):

$$\frac{D\epsilon_{\text{conduction}}}{Dt} \approx -\frac{1}{\rho} \nabla \cdot \left( 0.4 \left( \frac{2}{\pi m_e} \right)^{1/2} n_e (k_B T)^{3/2} \right) \quad (5)$$

### 3.2 Shock Propagation in the ICM

In general, propagation of a shock wave in a highly ionised plasma such as the ICM differs from that in an ordinary fluid because of the very different sound speeds for the electrons and ions. At the shock front, the ions undergo a temperature and density jump given by the normal Rankine-Hugoniot relations for a shock of Mach number  $M$ :

$$\frac{\rho_{2,\text{shock}}}{\rho_{1,\text{shock}}} = \frac{\gamma + 1}{(\gamma - 1) + \frac{2}{M^2}} \quad (6)$$

$$\frac{T_{2,\text{shock}}}{T_{1,\text{shock}}} = \frac{(2\gamma M^2 - (\gamma - 1)) (2 + (\gamma - 1)M^2)}{(\gamma + 1)^2 M^2} \quad (7)$$

Charge neutrality requires that the electrons are compressed adiabatically at the shock front in the same ratio as the ions, leading to a temperature difference:

$$T_i - T_e = \frac{T_{2,\text{shock}}}{T_{1,\text{shock}}} - \left( \frac{\rho_{2,\text{shock}}}{\rho_{1,\text{shock}}} \right)^{\gamma-1} \quad (8)$$

The two components are brought into thermal equilibrium behind the shock over a timescale comparable to their thermal equilibration time (Zel'Dovich & Raizer 1967):

$$\tau_{ei} \approx \frac{1.1 \times 10^{16} M A}{(n_i / \text{cm}^{-3}) Z^2 \ln \Lambda} \left( \frac{T}{\text{keV}} \right)^{3/2} \quad (9)$$

Where  $\tau_{ei}$  is the electron-ion equilibration timescale,  $A$  the atomic mass of the ions, and  $n_i$  the number density of ions. For the case of the Perseus cluster core with  $n_i \sim 0.03 \text{ cm}^{-3}$ ,  $T \sim 3.5 \text{ keV}$ ,  $\bar{A} = 1.29$ ,  $\bar{Z}^2 \approx \bar{Z}^2 = 1.2$  and  $M = 1.2$ , electron-ion equilibration occurs approximately 3.2 kpc behind the shock, consistent with the apparent offset between the temperature and density jumps at the shock front. In the case of a weak shock, however, the heating is largely due to adiabatic compression which acts equally on the electron and ion components and so from (8) the temperature difference is only  $\sim 1$  percent. Therefore electron-ion non-equilibration is unlikely to explain the observed density/temperature offset and we can approximate the behaviour of the ICM in the shocked region as that of a single-component fluid.

### 3.3 Conductivity of the ICM

In general the conductivity of the ICM may differ from the Spitzer value of equation (4) because even dynamically unimportant magnetic fields are effective in suppressing transport across field lines. Therefore the level of conductivity is strongly affected by the geometry of the field. In general it is assumed that the field is sufficiently tangled that, on scales of interest, isotropic conduction occurs due to motion of electrons along diverging field lines and so the conductivity is the Spitzer form reduced by some factor  $f < 1$ ; Narayan & Medvedev (2001) derive a suppression factor of  $f = 0.2$  based on the assumption of a tangled field. If the field is more ordered on smaller scales, the conduction will not be isotropic and parallel to the field lines the conductivity will be close to the full Spitzer value.

In the case of the ICM, there is some evidence of ordered field structures on scales  $>$  a few kpc. Surrounding many central cluster galaxies are bright, line emitting nebulae. In several cases including the Perseus (Conselice et al. 2001) and Centaurus clusters, long, largely radial, filamentary structures (up to 60 kpc in projection), are observed which are apparently long lived despite being embedded in the hot ICM (Fabian et al. 2003b; Hatch et al. 2005). In order to be stabilised against evaporation by the surrounding gas, thermal conduction between the filaments and their surroundings must be suppressed by about an order of magnitude more than in a tangled field (Nipoti & Binney 2004). This is suggestive of a field geometry in which the filaments are enclosed in a sheath of radially-coherent field lines.

Increasing radial coherence of the magnetic field toward the centre of the cluster is expected if there is radial flow of gas with a radially decreasing velocity amplitude, for example in a (reduced) cooling flow (Soker & Sarazin 1990). Recent numerical studies of bubbles evolution in a magnetised ICM has also shown the magnetic field becomes more ordered in the wake of the rising bubble (Ruszkowski et al. 2007b). With these results in mind, we assume that conduction may proceed radially at up to the full Spitzer rate.

### 3.4 Numerical Method

We have written the fluid equations (1) – (3) in a form appropriate to a one dimensional, spherically symmetric system:

$$\frac{dr}{dt} = u \quad (10)$$

$$\frac{du}{dt} = - \left( g + \frac{1}{\rho} \frac{dp}{dr} \right) \quad (11)$$

$$\frac{d\epsilon}{dt} = -p \frac{d}{dr} \left( \frac{1}{\rho} \right) - \frac{1}{\rho r^2} \frac{d}{dt} (r^2 q) \quad (12)$$

where  $q$  is the appropriate conductive heat flux. These are supplemented with the ideal gas equation of state:

$$p = \frac{\rho}{\mu m_H} k_B T \quad (13)$$

where we have taken the average particle mass  $\mu$  as a constant set to 0.61 appropriate to the chemical composition of the ICM.

To numerically solve these equations, we used an explicit finite difference method on a Lagrangian grid, based on the method of Ritchmyer & Morton (1967) and following the implementation of Morris (2003). An artificial viscosity term was added to the equation of motion to correctly model the shock jump conditions. The strength of the artificial viscosity was chosen so that the shock was smeared over approximately four grid zones.

For simplicity we neglect the contribution of the cluster galaxies to the gravitational acceleration and assume the contribution from gas is a fixed fraction of the dark matter contribution. Assuming the dark matter follows a NFW profile (Navarro et al. 1997), the acceleration may be written:

$$g_{\text{NFW}} = \frac{GM_{\text{virial}} \log(1 + cr/r_{\text{virial}}) - cr/(r_{\text{virial}} + cr)}{r^2 \log(1 + c) - c/(1 + c)}, \quad (14)$$

where  $M_{\text{virial}}$  and  $r_{\text{virial}}$  are the virial mass and radius respectively and  $c$  is the cluster concentration.

The shock wave was generated by moving the position of the inner boundary. If the jet supplies energy at a constant rate  $\dot{E}$  then it can be shown that the bubble radius varies with time as:

$$R_b = \left( \frac{\dot{E} t^3}{\rho} \right)^{\frac{1}{5}}. \quad (15)$$

Numerically this formulation is problematic as it requires a high (formally infinite) velocity at  $t = 0$ . Instead we have adopted a simpler model with an initial exponential increase in the expansion velocity to a maximum and a subsequent fall off like  $\cos(t)$ :

$$u_{\text{piston}} = \begin{cases} u_0 \left( \frac{\exp(t/t_{\text{smooth}}) - 1}{e - 1} \right) & 0 < t < t_{\text{smooth}} \\ u_0 \cos \left( \frac{2\pi}{t_p} (t - t_{\text{smooth}}) \right) & t_{\text{smooth}} < t < t_{\text{max}} \\ 0 & t > t_{\text{max}} \end{cases} \quad (16)$$

The smoothing time  $t_{\text{smooth}}$  has been fixed at 1 Myr; with this time, no spurious central heating due to sharp changes in velocity are observed.  $t_p$  is a characteristic piston timescale and  $u_0$  defines the maximum piston velocity. Since we are concerned with only a single injection event, we choose  $t_{\text{max}}$  to occur when the piston velocity first reaches zero, i.e.  $t_{\text{max}} = t_{\text{smooth}} + t_p/4$ .

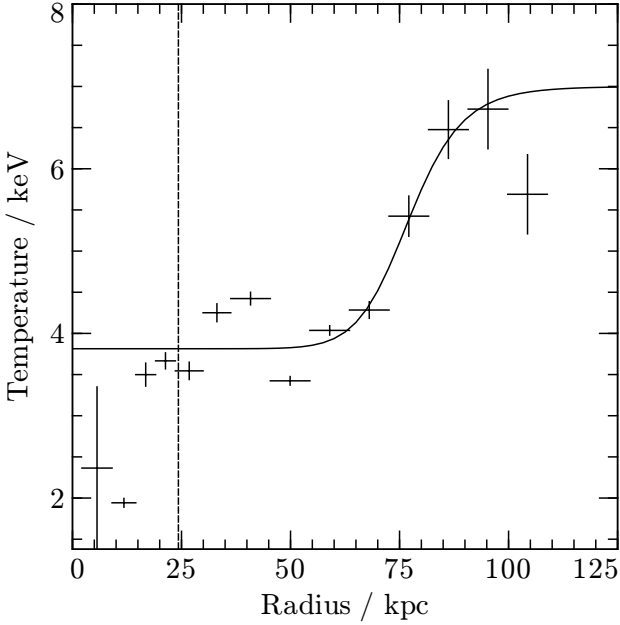


**Figure 6.** Deprojected temperature data from the 200ks observation (Sanders et al. 2004) for a sector of the Perseus cluster containing the shock (points) and adopted initial temperature profile (line). The sector used contains the four regions covering the shock in Fig. 18 of (Sanders et al. 2004). This region is similar to that in Fig. 1 but has a significantly greater radial extent. The vertical line shows the approximate position of the shock.

## 4 COMPARISON WITH DATA

### 4.1 Initial Conditions

As we are primarily concerned with modelling the observed shock in the Perseus cluster, the majority of our models are set up with properties close to those of the NE sector of the Perseus cluster used in the deprojection analysis. Our initial temperature profile was based on the observed temperature in the pre-shock region (i.e.  $r > 20$  kpc). To determine the shape of the profile at large radii, we used a fit to the 200 ks data presented in Sanders et al. (2004) covering the shock region, whilst the temperature in the immediate vicinity of the shock was matched to the data in Fig. 3. The resulting profile, together with the Sanders et al. (2004) data is shown in Fig. 6. The functional form is:

$$T = 7 \frac{1 + \left(\frac{r}{73 \text{ kpc}}\right)^{14}}{1.93 + \left(\frac{r}{73 \text{ kpc}}\right)^{14}} \text{ keV} \quad (17)$$

The gravitational acceleration was modelled using the NFW component of the profile in Mathews et al. (2006), which provides an acceptable fit to the observed acceleration in the region  $r > 10$  kpc which is of interest here. The initial density profile is calculated assuming hydrostatic equilibrium and a central density  $n_e = 0.05 \text{ cm}^{-3}$ . This gives a gas mass fraction inside 25 kpc of  $\sim 6\%$ , so a static gravitational field is expected to be a good approximation. The piston timescale  $t_p$  was taken as  $1 \times 10^7$  yr and the smoothing time as  $1 \times 10^6$  yr.

The inner boundary was started at  $r = 5$  kpc — approximately the distance from the bubble centre to the cluster centre — and the piston amplitude adjusted to  $r_{\text{piston}} = 3$  kpc so that the

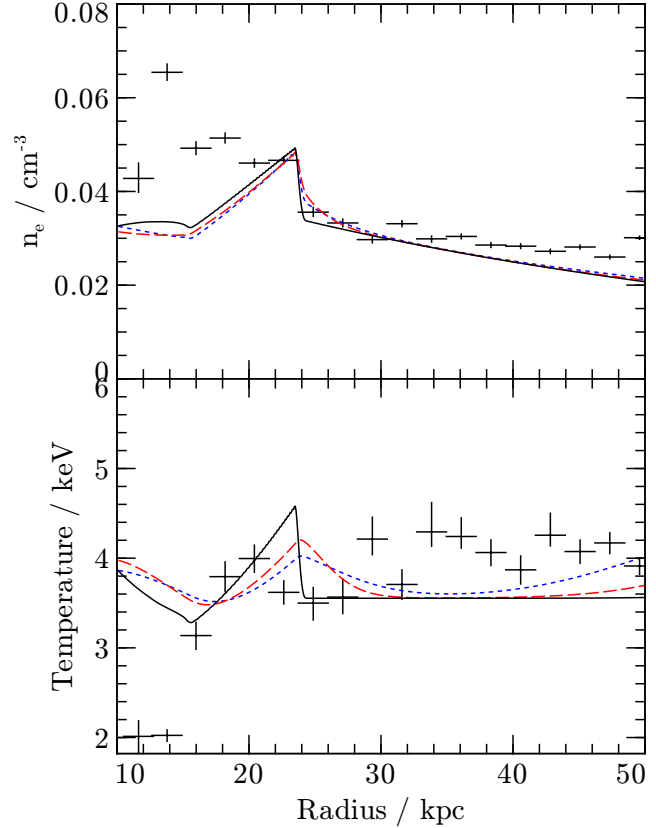


**Figure 7.** Density and temperature after the shock has reached 24 kpc with  $\gamma = \frac{5}{3}$  and no conduction (solid line), a Spitzer fraction of 1.0 (dashed line) and 2.0 (dotted lines) and deprojected observations in the NE sector (points).

shock approximately reproduced the expected density jump at the current shock position.

When adding conduction to the models, Spitzer fractions,  $f$ , in the range 0-2 have been considered. Cases with the conductivity in excess of the Spitzer value are intended as a simple approximation for a situation where the electrons and ions are decoupled. In this case only  $\sim 1/2$  of the energy needs to be transported to decrease the observed (electron) temperature compared with the fully coupled case.

### 4.2 Simulation Results

For the purposes of comparison with the simulations, we have used radii measured from the cluster centre rather than from the centre of the deprojected sector, since this more closely matches the setup of the simulated cluster. The radius of the shock is then 24 kpc.

Fig. 7 shows the density and temperature structure of a simulation with  $\gamma = 5/3$  after the shock has reached the observed radius (taken to be 24 kpc). The time taken for this to occur was dependent on the level of conduction; in the non conductive case the time was  $\sim 12$  Myr, stronger conduction reduces the pressure difference across the shock so slowing its propagation. The piston amplitude was adjusted so that the observed density jump was matched in each case. The addition of conduction with  $f = 1$  and  $f = 2$  reduces the height of the jump to about 65 percent and 50 percent respectively of the non-conductive case. However conduc-

$\gamma$	Model Parameters		Fitting results	
	$r_p$ / kpc	$t_p / 10^7$ yr	$f$	Reduced $\chi^2$
5/3	2.75	1	0	7.4
5/3	3	1	1	5.6
5/3	3	1	2	4.1
3/2	2.5	1	0	3.7
3/2	2.5	1	1	3.4
3/2	2.5	1	2	3.1
4/3	2.5	1	0	2.3
4/3	2.6	1	1	2.6
4/3	2.6	1	2	2.4
5/3	2.75, 2	1,1	0	10.7
5/3	3, 2	1,1	1	7.7
5/3	3, 2	1,1	2	5.7

**Table 1.** Results of numerical simulations for various values of  $\gamma$ , the Spitzer fraction  $f$  and numbers of injection events. The piston amplitude  $r_p$  is adjusted so that the density jump at 24 kpc matches the observations. The quoted reduced chi-squared is based on a fit of the temperature data alone to the five data points in the region 18 – 28 kpc enclosing the shock front.

tion does not appear to change the position of the temperature jump relative to the density jump.

A more quantitative comparison of the data and the models can be made by performing a  $\chi^2$  fit of the model temperature profile to the data in the region surrounding the shock. To allow for the fact that the data shows more structure ahead of the shock than the initial conditions of our model, we have selected only those data points in the region 18 kpc  $\leq r \leq$  28 kpc and spectrally averaged the model temperatures to match the data bins. A simple fit of the models to the data products a rather poor fit in each case with the reduced  $\chi^2$  ranging from 4.1 in the case  $f = 2$  to 7.2 in the case  $f = 0$ . The quality of the fit also depend somewhat on the initial temperature profile assumed. For example, maintaining the shape of the profile but increasing the central value makes the fits poorer in all cases.

We have also considered models in which the ratio of specific heats is less than the standard ideal gas value of 5/3. Lower values of  $\gamma$  may be appropriate if the ICM in the neighbourhood of the shock is significantly contaminated by relativistic particles diffusing from the bubbles (Mathews & Brighenti 2007; Ruszkowski et al. 2007a). In this case the effective adiabatic index is given by:

$$\gamma_{\text{eff}} = \frac{\gamma_{\text{Th}} + X_{\text{CR}}\gamma_{\text{CR}}}{1 + X_{\text{CR}}} \quad (18)$$

with  $X_{\text{CR}} = p_{\text{CR}}/p_{\text{Th}}$  (Pfrommer et al. 2007). We consider  $\gamma = 4/3$  as a limiting case of cosmic-ray-pressure dominated gas and  $\gamma = 3/2$ , i.e.  $X_{\text{CR}} = 1$ , as a realistic value for the core of the Perseus cluster based on the analysis of the non-thermal emission by Sanders & Fabian (2007).

The temperature profiles for the  $\gamma = 4/3$  case are shown in Fig. 8. As expected from the standard shock jump conditions, the magnitude of the shock in the is substantially decreased compared to the  $\gamma = 5/3$  case. However conduction appears to show little further effect in this case. The reduced  $\gamma$  appears to somewhat improve the agreement between simulation and data but does not produce a statistically acceptable fit in either case.

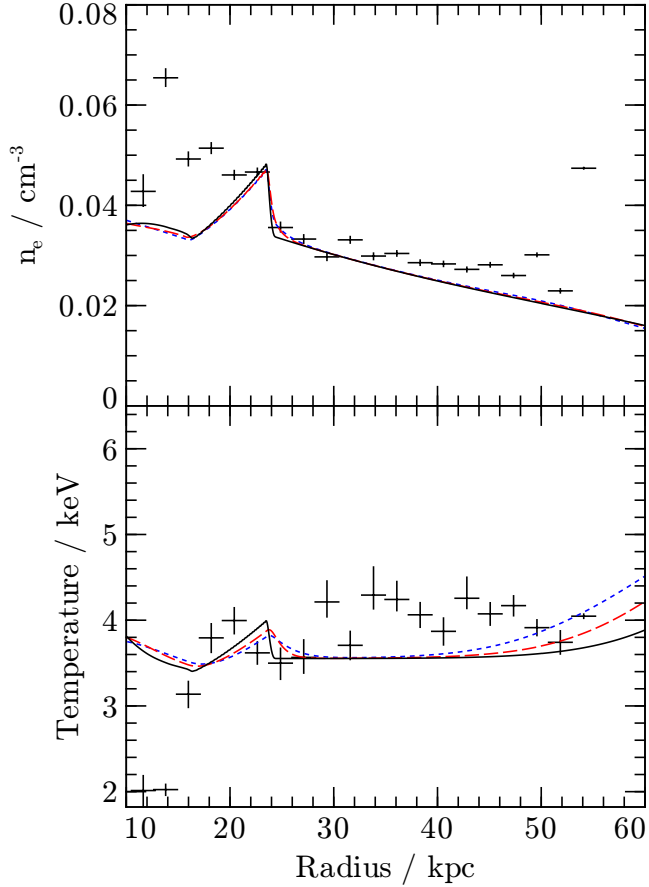


**Figure 8.** Shock model at  $r = 24$  kpc for the Perseus-like model cluster with  $\gamma = \frac{4}{3}$  and no conduction (solid line), a Spitzer fraction of 1.0 (dashed line) and 2.0 (dash-dotted line).

#### 4.2.1 Models with Multiple Consecutive Outbursts

By construction our models match the density and the density jump at the shock front. Nevertheless, the models considered so far all show high density regions inside the shock considerably narrower than that observed.

One way of addressing this issue is to invoke multiple outbursts during a single cycle of AGN activity. Fig. 9 shows the density and temperature profiles for set of models in which the single outburst has been replaced by two identical outbursts beginning at  $t = 0$  and  $t = 4.5$  Myr.

This model successfully reproduces a thicker rim of high density gas that extends in approximately as far as the obscuring cool gas seen in the data, although it tends to produce a somewhat worse fit to the temperature profile than the single-outburst models.

#### 4.3 The Temperature Offset

Since our simulations do not convincingly reproduce a temperature/density offset at the shock front, we must consider other mechanisms for cooling the gas in the immediate aftermath of the shock.

##### 4.3.1 Non-Uniform Initial Temperature

We have assumed a temperature profile that is flat in the core of the cluster. However the deprojected temperature profile shows ev-

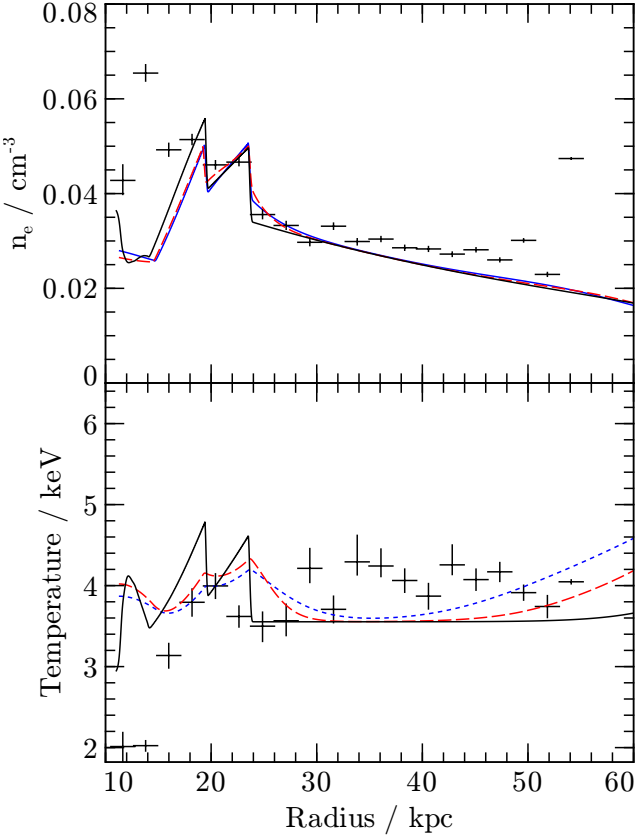


**Figure 9.** Temperature profile for a model with two episodes of injection starting at  $t = 0$  and  $4.5 \times 10^6$  with  $r_p = 3$  kpc and 2 kpc respectively and  $t_p = 1 \times 10^7$  yr in each case.

idence for oscillations in the temperature of up to  $\sim 0.5$  keV. A blob of cold gas producing a temperature fluctuation of around this magnitude at the position of the observed density jump can produce density and temperature profiles similar to the observed ones—a simulation of such a profile is seen in Fig. 10. However this relies on fine-tuning of the initial temperature profile, suggesting that weak shocks in general would not show such an offset. However, the very high resolution observations required to test this are only likely to be possible for a very small number of local clusters in the foreseeable future.

#### 4.3.2 Mixing of Filaments

Thus far, we have ignored the multiphase nature of the Perseus core in our analysis. Of particular significance is the reservoir of cool gas contained in the large filamentary nebula associated with the central cluster galaxy. However, there is observational evidence for an interaction between the phases; Fig. 11 shows the X-ray pressure and  $H\alpha$  map around the region we have analysed. The filaments in this region appear to terminate at the shock front, suggesting the cool gas from the filaments is being mixed in with the hot ICM in this region. This mixing could have a significant impact on the temperature structure of the shock.

The filaments are known to contain  $H_2$  with a temperature of  $300 - 10000$  K and a mass per unit length of around  $10^4 - 10^5 M_\odot / \text{kpc}$  (Johnstone et al. 2007). Associated with the filaments is soft X-ray emission (Fabian et al. 2003b), tracing a to-

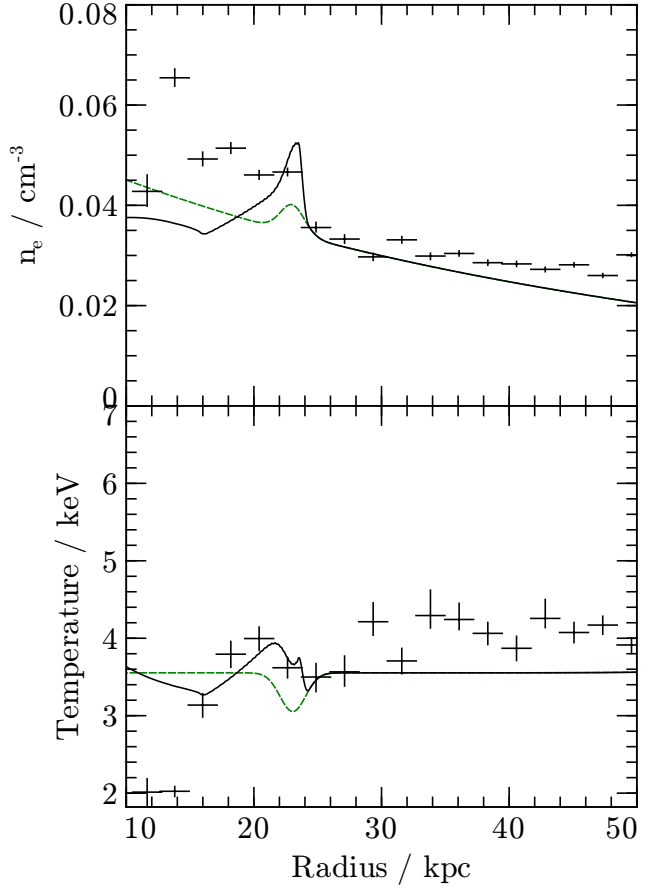


**Figure 10.** Density (top) and temperature (bottom) profiles at  $t = 0$  (dashed lines) and  $t = 13$  Myr (solid lines) for a model with a blob of colder gas close to the observed shock radius.

tal mass of  $\sim 10^9 M_\odot$  within the inner 1.5 arcmin ( $\sim 33$  kpc) (Fabian et al. 2006). There is also a detection of CO in the region of the filaments (Salomé et al. 2006), implying a population of gas at 10-100K, although it is not clear if this is confined to the filaments or more dispersed. If it is indeed confined to the filaments it implies a mass per unit length of around  $10^8 M_\odot / \text{kpc}$ . The density of the X-ray emitting gas in the region of the shock is approximately  $7 \times 10^5 M_\odot / \text{kpc}^3$  so, assuming complete mixing of the gas behind the shock, a single filament could cool around  $1000 \text{ kpc}^2$  of the shock front by 0.5 keV, an area comparable to the surface area of a spherical shock centred on the Perseus bubbles and at the observed radius. However, in practice the efficiency of mixing is likely to be considerably less than 100 percent, so this estimate is an upper bound.

If the post-shock gas is cooled by mixing of filaments, then we might expect a spatial variation in the post-shock temperature according to the distribution of filaments along the shock front. Fig. 12 shows the deprojected density and temperature profiles when the sector in Fig. 1 is divided into two equal-angle sectors. Outside the shock front the two profiles are consistent, but inside the shock there is a significant difference in the temperatures for the two sectors; one is consistent with a flat temperature profile whilst the other has a jump of  $1.36 \pm 0.13$  between the preshock minima and post-shock maxima. Interestingly, it is the sector closer to the currently observed filaments that has the larger temperature jump; this may

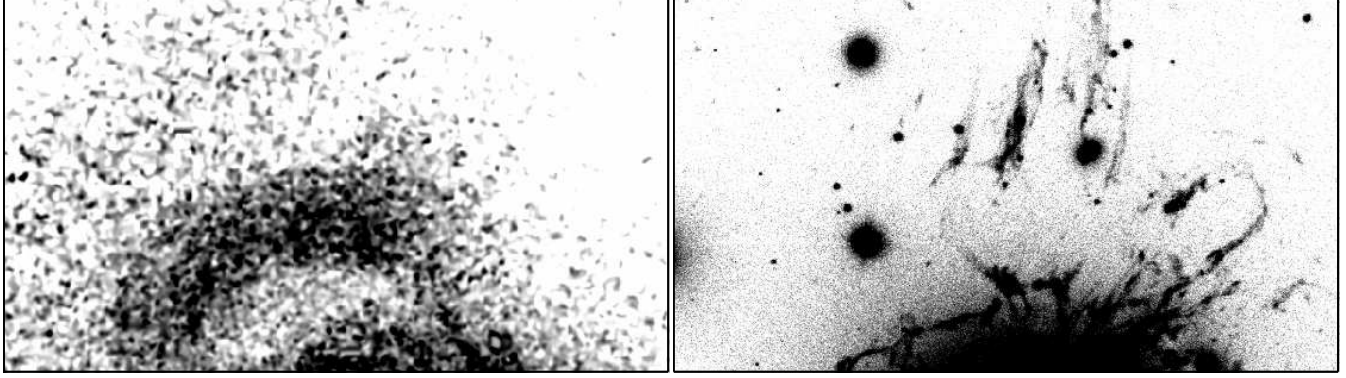


**Figure 11.** X-ray pressure (Fabian et al. 2006, left) and H $\alpha$  (Conselice et al. 2001, right) maps for a 150  $\times$  80 arcsecond region in the north of the Perseus cluster. The filaments in the H $\alpha$  map appear to terminate at the shock front in this region

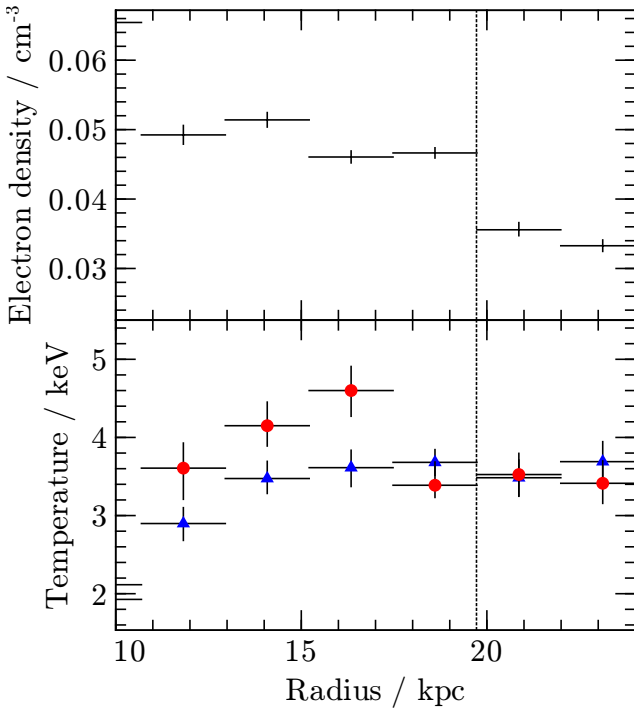


**Figure 12.** Full sector density profile (top) and split sector temperature profiles (bottom). The vertical line marks the position of the shock. The circular points are for the NW most half of the original sector and the triangular points for the SE. A jump in temperature behind the shock front is seen only for the NW-most sector.

be indicative of the shock having destroyed previous filaments in the cooler sector.

Assuming the filaments have had a significant effect on the temperature structure of the gas, it is not clear why the postshock temperature should be roughly the same as the preshock temperature; by mixing more or less cold gas into the ICM this could be varied from the postshock temperature expected from the Rankine-Hugoniot relations to a temperature significantly lower than the preshock temperature. A physical mechanism to explain the near-isothermality observed would make this model significantly more appealing.

#### 4.4 Repeated Shock Heating

We now briefly address the issue of repeated shock heating of the cluster core. Previous authors (Mathews et al. 2006; Fujita & Suzuki 2006), have found that repeated shocking of the cluster core leads to a centrally increasing temperature profile, clearly inconsistent with the observations. This is a result that we can reproduce in our model; Fig. 13 shows the result of repeatedly shocking a cluster, with the initial conditions identical to those employed for the models of the Perseus shock, over a period of 4 Gyr with wave parameters  $r_p = 2.75$  kpc,  $t_p = 2 \times 10^7$  yr and  $r_{\min} = 10$  kpc. Clearly the temperature profile produced is not the smoothly decreasing temperature profile we expect from observations.

However, we recommend caution in a literal interpretation of these results derived from these 1D models. There are several limitations of the models that may cause the discrepancy between the model and the data:

- The 1D nature of the models misses several essential features of real clusters. The geometry of bubble heating in 3D allows the redistribution of material from outside the bubble into the core of the cluster and conversely the entrainment of the material behind the rising bubble draws material away from the centre (e.g. Gardini 2007). Changes in the jet direction and bulk motion of the ICM in the cluster potential are also significant effects in ensuring that the same cluster gas is not repeatedly subject to the strongest heating, as happens in the 1D case (Brüggen et al. 2005; Heinz et al. 2006).

- The assumption of constant piston amplitude (“bubble size”) over time is likely to be unrealistic. One would expect a real source to release bubbles with a variety of sizes over a variety of timescales. Evidence of this in the Perseus cluster is seen in the spatial variation of the ripple amplitude reported by Sanders & Fabian (2007). In addition to changes in the intrinsic power of the central source, the bubble size and release frequency, at constant power, will vary with the surrounding gas properties. However the weakness of this dependence means this is likely to be an insignificant effect.

- Models to date have taken no account of the possibility of the mixing of cool gas from the brightest cluster galaxy nebula into the ICM. We have shown that this process may plausibly have an effect on the temperature structure of the weak shock in Perseus, in which case it will alter the temperature structure produced by repeated heating episodes.

- A non-homogeneous population of cosmic rays will affect

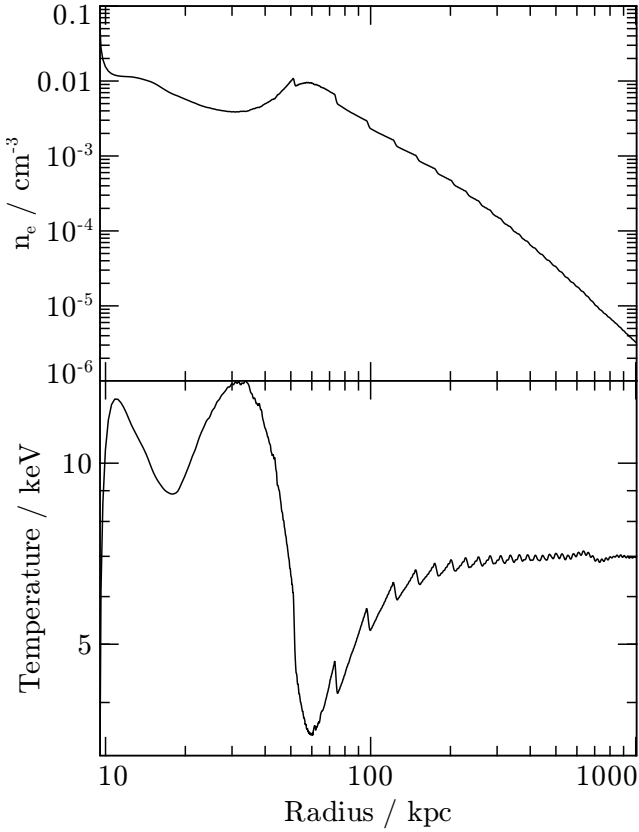


**Figure 13.** Density and temperature profiles for a simulation in which a Perseus-like cluster is subject to monochromatic wave heating for 4 Gyr. The central temperature peak is characteristic of this kind of simulation but is inconsistent with the data.

how the energy dissipated by weak shock waves is distributed spatially.

In order to resolve these issues, it is clear that simulations with repeated bubble formation events run over a period of several Gyr in multiple dimensions are required. Dalla Vecchia et al. (2004) have run a 3D simulation for 1.5 Gyr in which they are able to balance heating and cooling, although their results are dependent on the radius over which their bubbles are distributed, with small injection radii (consistent with observations) leading to a potentially problematic increase in energy of the cluster core. However their simulation contains neither bulk gas motion nor the inflation of the bubbles themselves. Sijacki et al. (2007) have also run a cosmological simulation including mechanical feedback from AGN, with the energy and radius of the bubbles coupled to the black hole accretion rate. They find the injection is able to prevent catastrophic cooling in the cluster core, whilst retaining a flat or decreasing temperature profile in the centre.

## 5 ENERGETICS OF THE SHOCKED REGION

The amount of mechanical energy imparted to the cool core region by the AGN is critical in determining whether the AGN alone can offset the cooling flow to the observed levels in cluster cores. If the bubble is slowly inflated and thereafter expands adiabatically as it rises buoyantly through the cluster core, it releases an energy of approximately  $(\gamma_{\text{bubble}}/(\gamma_{\text{bubble}} - 1))pV$ , i.e. its enthalpy

(Churazov et al. 2002). Therefore studies of AGN heating have typically assumed  $E = 4pV_{\text{observed}}$ , appropriate if the gas inside the bubble is purely relativistic. With these assumptions, authors have typically found that the available energy is enough to offset the cooling in some but not all clusters (e.g. Bîrzan et al. 2004; Dunn & Fabian 2006; Rafferty et al. 2006; Bîrzan et al. 2006). The fraction of clusters for which heating is observed to balance cooling at the present time is often used to infer a duty cycle for mechanical energy input by the AGN.

Some simulations have suggested that the overall energy release is substantially greater than assumed in these studies due to the contribution from non-adiabatic processes (e.g. Binney et al. 2007). The high quality data from the Perseus allow us to see the high pressure rims around the inner bubbles, allowing an observational estimate of the extra energy deposited by irreversible processes during the bubble expansion.

Following Dunn et al. (2005) we assume that the Perseus bubbles are approximately spherical, of radius  $r_{\text{inner}}$  and that the shocked material is confined to a spherical shell of radius  $r_{\text{outer}}$  outside each bubble. The energy dissipated by the shock is then:

$$E_{\text{shock}} = \frac{1}{\gamma_{\text{gas}} - 1} \iiint_{\text{shell}} (p_{\text{shocked}} - p_{\text{unshocked}}) dV \quad (19)$$

The value of  $p_{\text{unshocked}}$  is, of course, an unknown quantity, which we must extrapolate from the properties of the cluster outside the shock. In order to minimise the uncertainty associated with this extrapolation, we assume that both bubbles are identical and that the pressure profile through the whole region surrounding the bubble, both inside and outside the shock, is well approximated by the profile in that region in the sector we have studied in this paper. With these assumptions we only need extrapolate the pressure profile over the width of the high pressure region. To perform this extrapolation, we use a power-law fit to the pressure profile in the range 20 – 45 kpc, measured from the bubble centre:

$$p_{\text{unshocked}} = 0.40 \left( \frac{r}{1 \text{ kpc}} \right)^{-0.16} \text{ keV cm}^{-3}, \quad (20)$$

For the shocked pressure we used the values measured in the high pressure region  $r = 10.1 - 19.3$  kpc directly (where  $r$  is measured from the centre of the bubble as in Fig. 3). With these parameters, the excess energy in the high pressure shell is  $1.6 \times 10^{59}$  erg per bubble. If we estimate the power provided by the shock as  $E_{\text{shock}}/t_{\text{shock}}$  where  $t_{\text{shock}} = (r_{\text{outer}} - r_{\text{inner}})/Mc$ , we find  $P_{\text{shock}} \sim 6 \times 10^{44}$  erg s<sup>-1</sup> per bubble.

From Dunn & Fabian (2004), the  $pV$  work done in expanding the bubbles adiabatically are  $3.9 \times 10^{58}$  erg and  $5.3 \times 10^{58}$  erg for the northern and southern bubbles, respectively. Therefore, averaging over the two bubbles, we find that the energy in the shocked region is roughly 3.5 times the  $pV$  work done in expanding the bubbles adiabatically, already comparable to the enthalpy of the bubbles. Assuming this result generalises to other clusters, estimates of the total AGN-supplied mechanical power available to heat cluster cores which assume  $4pV$  energy per bubble over their lifetime are likely to be reliable.

The calculated power is somewhat higher than the range  $6 \times 10^{43} - 2 \times 10^{44}$  erg s<sup>-1</sup> per bubble found by Dunn & Fabian (2004) on the basis of the work done expanding the bubbles (i.e. taking the energy to be  $pV$ , not  $4pV$ ) and various estimates of the timescale for energy dissipation. It is also comparable to, although,

again, slightly larger than, the power in the ripples calculated by Sanders & Fabian (2007).

These estimates have all been made on the assumption that only the thermal pressure is significant. Sanders & Fabian (2007) found that inside 40 kpc Perseus has a significant non-thermal pressure component contributing about 50 percent of the thermal pressure. Therefore the energy inside the shocked region may be an additional factor  $\sim 1.5$  higher than derived here.

It is also possible that excess energy has been channelled into other modes such as gravitational energy, kinetic energy or turbulence. We expect the contribution of gravitational energy to be small; assuming the expansion is approximately symmetric, the almost linear nature of the cluster potential over the region  $r < r_{\text{outer}}$  means that the net change in the gravitational potential cancels. Relaxing the condition of symmetrical redistribution, the condition of hydrostatic equilibrium gives  $\Delta P \sim \rho g \Delta r$  so  $E_{\text{grav}}/E_{\text{thermal}} \sim \Delta P/P \sim 0.1$  therefore the gravitational contribution to the total energy is likely to be small.

## 6 DISCUSSION AND CONCLUSIONS

We have performed a detailed analysis of the weak shock feature seen in the core of the Perseus cluster. Deprojection of a sector containing the shock shows no temperature rise coincident with the density jump. There is a small rise 3 kpc downstream from the shock front. Models of shock production in spherically-symmetric, ideal gas, cluster atmospheres produce poor fits to the observed profile, principally because the observed postshock temperature is lowest at the shock front, just where it is expected to be highest.

The presence of thermal conduction, or a reduced value of the adiabatic index from the presence of a population of cosmic rays, can produce a temperature jump with very similar magnitude to that seen in the data and substantially improve the fit of the shock profile to the data. However we did not find a set of parameters for which the  $\chi^2$  value of the fit is statistically acceptable. The difficulty of finding a simple solution to this problem is likely related to the fact that the densities and length scales relevant to the Perseus shock represent the border between the collisional and collisionless regimes. Therefore the non-hydrodynamic physics, such as the interaction of the electron population with the local magnetic field, may be essential to the formation of the observed structures.

Mixing of cold gas may have a significant effect on the energy distribution in all cool core clusters. Of the nearby large cooling flows, it is only Abell 2029 which does not show evidence for a large filamentary nebula (Johnstone et al. 1987). In the Virgo cluster, where both  $\text{H}\alpha$  filaments (Sparks et al. 2004) and a weak shock (Forman et al. 2007) are seen, the shock is outside the region of strong filamentary emission. Unlike Perseus, there is no evidence of deviation from the standard Rankine-Hugoniot relations for the shock in Virgo.

Finally, we must consider the possibility that the pressure across the density jump is in fact continuous with an increase in the thermal gas pressure fraction in the ‘‘preshock’’ region. This could be the case if the medium outside the front has a larger component of ram, magnetic field or cosmic ray pressure, for example.

The geometry of the density jump seems to disfavour an increase in ram pressure; because the shock is a continuous feature around the inner region it is difficult to maintain a bulk flow of the material in the whole outer region.

The viability of the observed feature being produced by a change in the magnetic field strength across the density front de-

pends greatly on the field strength in the inner region. Taylor et al. (2006) find a magnetic field of around  $25 \mu\text{G}$  based on rotation measure measurements of the very inner regions of the cluster core, although they suggest this field is associated largely with the filamentary nebula, whilst Sanders et al. (2005) estimate a magnetic field of around  $0.1 \mu\text{G}$  from non-thermal X-ray emission. In order to provide a continuous pressure across the shock, we require  $B_{\text{outer}}^2 - B_{\text{inner}}^2 \sim 6 \times 10^3 \mu\text{G}^2$ . If the inner field is around  $25 \mu\text{G}$  this is a factor of around 3 increase in the field strength. For a smaller outer field the required increase is correspondingly larger and for a  $0.1 \mu\text{G}$  inner field, magnetic pressure balance across the density front would require an implausible increase in the field strength of a factor of  $\sim 1000$ .

If there were a significant change in either the magnetic field or non-thermal particle population in the gas moving across the density front, we would expect to see a corresponding feature in the radio mini-halo emission. No such feature can obviously be identified in the VLA data of Sijbring (1993), although we cannot entirely rule out a model in which the non-thermal gas is the largest fraction by volume and the ‘‘shock’’ feature is associated with a change in the number density of clouds of thermal gas. Nevertheless, the difficulties associated with these constant pressure models lead us to believe that an outward-propagating weak shock wave is the most likely explanation for the observed feature.

In conclusion, the high pressure regions surrounding the inner radio bubbles in the Perseus cluster terminate in spherical shocks. The density jumps by 31 percent at the shock front, yet any immediate temperature jump is only  $3 \pm 6$  percent. This is inconsistent with a simple adiabatic shock. We are unable to find a definitive solution to the problem. Several possibilities have been investigated, with turbulent post-shock gas rapidly mixing with cool material associated with the optical filaments being promising. Such mixing, and the 3D geometry of the bubbles, can prevent the central gas from overheating, despite repeated bubbling over hundreds of millions of years. The excess thermal energy contained in these high pressure region is about 3.5 times the total work done in expanding the bubbles adiabatically and the power provided by the shock is enough to significantly offset the cooling in Perseus.

## 7 ACKNOWLEDGEMENTS

JG and ACF acknowledge support from the Science and Technology Facilities Council and the Royal Society, respectively.

## REFERENCES

- Binney J., Bibi F. A., Omma H., 2007, MNRAS, 377, 142
- Bîrzan L., McNamara B. R., Carilli C. L., Nulsen P. E. J., Wise M. W., 2006, astro-ph/0612393
- Bîrzan L., Rafferty D. A., McNamara B. R., Wise M. W., Nulsen P. E. J., 2004, ApJ, 607, 800
- Borkowski K. J., Leyerly W. J., Reynolds S. P., 2001, ApJ, 548, 820
- Borkowski K. J., Sarazin C. L., Blondin J. M., 1994, ApJ, 429, 710
- Brüggen M., Ruszkowski M., Hallman E., 2005, ApJ, 630, 740
- Churazov E., Sunyaev R., Forman W., Böhringer H., 2002, MNRAS, 332, 729
- Conselice C. J., Gallagher J. S., Wyse R. F. G., 2001, AJ, 122, 2281

Cowie L. L., McKee C. F., 1977, *ApJ*, 211, 135

Dalla Vecchia C., Bower R. G., Theuns T., Balogh M. L., Mazzotta P., Frenk C. S., 2004, *MNRAS*, 355, 995

Dunn R. J. H., Fabian A. C., 2004, *MNRAS*, 355, 862

Dunn R. J. H., Fabian A. C., 2006, *MNRAS*, 373, 959

Dunn R. J. H., Fabian A. C., Taylor G. B., 2005, *MNRAS*, 364, 1343

Fabian A. C., 1994, *ARA&A*, 32, 277

Fabian A. C., Sanders J. S., Allen S. W., Crawford C. S., Iwasawa K., Johnstone R. M., Schmidt R. W., Taylor G. B., 2003a, *MNRAS*, 344, L43

Fabian A. C., Sanders J. S., Crawford C. S., Conselice C. J., Gallagher J. S., Wyse R. F. G., 2003b, *MNRAS*, 344, L48

Fabian A. C., Sanders J. S., Taylor G. B., Allen S. W., Crawford C. S., Johnstone R. M., Iwasawa K., 2006, *MNRAS*, 366, 417

Forman W. et al., 2007, *ApJ*, 665, 1057

Fujita Y., Suzuki T. K., 2006, ArXiv Astrophysics e-prints

Gardini A., 2007, *A&A*, 464, 143

Hamilton A. J. S., Chevalier R. A., Sarazin C. L., 1983, *ApJS*, 51, 115

Hatch N. A., Crawford C. S., Fabian A. C., Johnstone R. M., 2005, *MNRAS*, 358, 765

Heinz S., Brüggen M., Young A., Levesque E., 2006, *MNRAS*, 373, L65

Johnstone R. M., Fabian A. C., Nulsen P. E. J., 1987, *MNRAS*, 224, 75

Johnstone R. M., Hatch N. A., Ferland G. J., Fabian A. C., Crawford C. S., Wilman R. J., 2007, *MNRAS*, 1005

Landau L. D., Lifshitz E. M., 1959, Fluid mechanics. Course of theoretical physics, Oxford: Pergamon Press, 1959

Liedahl D. A., Osterheld A. L., Goldstein W. H., 1995, *ApJ*, 438, L115

Mathews W. G., Brighenti F., 2007, *ApJ*, 660, 1137

Mathews W. G., Faltenbacher A., Brighenti F., 2006, *ApJ*, 638, 659

Morris R., 2003, Ph.D. thesis, University of Cambridge

Narayan R., Medvedev M. V., 2001, *ApJ*, 562, L129

Navarro J. F., Frenk C. S., White S. D. M., 1997, *ApJ*, 490, 493

Nipoti C., Binney J., 2004, *MNRAS*, 349, 1509

Peterson J. R., Kahn S. M., Paerels F. B. S., Kaastra J. S., Tamura T., Bleeker J. A. M., Ferrigno C., Jernigan J. G., 2003, *ApJ*, 590, 207

Peterson J. R. et al., 2001, *A&A*, 365, L104

Pfrommer C., Enßlin T. A., Springel V., Jubelgas M., Dolag K., 2007, *MNRAS*, 430

Rafferty D. A., McNamara B. R., Nulsen P. E. J., Wise M. W., 2006, *ApJ*, 652, 216

Ritchmyer R. D., Morton K. W., 1967, Difference methods for initial-value problems. Interscience Tracts in Pure and Applied Mathematics, New York: Interscience, 1967, 2nd ed.

Ruszkowski M., Enßlin T. A., Brüggen M., Begelman M. C., Churazov E., 2007a, ArXiv e-prints, 705

Ruszkowski M., Enßlin T. A., Brüggen M., Heinz S., Pfrommer C., 2007b, *MNRAS*, 378, 662

Salomé P. et al., 2006, *A&A*, 454, 437

Sanders J. S., Fabian A. C., 2007, *MNRAS*, 381, 1381

Sanders J. S., Fabian A. C., Allen S. W., Schmidt R. W., 2004, *MNRAS*, 349, 952

Sanders J. S., Fabian A. C., Dunn R. J. H., 2005, *MNRAS*, 360, 133

Sijacki D., Springel V., di Matteo T., Hernquist L., 2007, *MNRAS*, 380, 877

Sijbring D., 1993, Ph.D. thesis, Groningen

Soker N., Sarazin C. L., 1990, *ApJ*, 348, 73

Sparks W. B., Donahue M., Jordán A., Ferrarese L., Côté P., 2004, *ApJ*, 607, 294

Spitzer L., 1956, Physics of Fully Ionized Gases. Physics of Fully Ionized Gases, New York: Interscience Publishers, 1956

Taylor G. B., Gugliucci N. E., Fabian A. C., Sanders J. S., Gentile G., Allen S. W., 2006, *MNRAS*, 368, 1500

Zel'Dovich Y. B., Raizer Y. P., 1967, Physics of shock waves and high-temperature hydrodynamic phenomena. New York: Academic Press, 1966/1967, edited by Hayes, W.D.; Probstein, Ronald F.